ACS OMEGA

Open Access

http://pubs.acs.org/journal/acsodf

Article

One-Pot Fabrication of Copper-Doped $WO_3 \cdot H_2O$ Opto-Functional Layered Device using Submerged Photosynthesis of Crystallites

Mahiro Nishimura, Hiroto Miyashita, Hsueh-I Lin, Lihua Zhang, Melbert Jeem, and Seiichi Watanabe*

Cite This: *ACS Omega* 2024, 9, 44714−44723

Read Online

ACCESS | Metrics & More | Article Recommendations | Supporting Information

ABSTRACT: This study introduces a one-pot, submerged photosynthesis of crystallites (SPsC) method for fabricating monohydrate tungstic acid ($WO_3 \cdot H_2O$) nanoplates directly integrated onto a stainless steel mesh, offering a simplified production and enhanced device stability for optical functional applications. The fabricated devices demonstrate exceptional broadband light absorption across the ultraviolet (UV), visible (Vis), and near-infrared (NIR) ranges. Notably, 1% Cu doping significantly boosts the NIR absorption, yielding a high solar utilization efficiency of 81.40%. In solar water evaporation experiments, the devices exhibit a maximum temperature increase of 13 °C under 1-Sun (100 mW/cm^2) illumination, achieving an energy conversion efficiency of 32.5%. Moreover, electrochemical characterization reveals light-induced conductivity changes and enhanced current density, suggesting potential applications in rectifying devices. This versatile and environmentally conscious SPsC fabrication method holds promise for the sustainable development of diverse nanodevices.

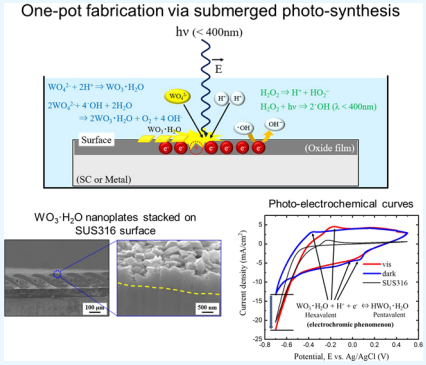

1. INTRODUCTION

The escalation of global challenges, including energy scarcity, resource depletion, and environmental degradation, necessitates immediate and sustainable solutions. Renewable energy sources have thus gained attention for their potential to provide sustainable and reliable energy. Solar energy is particularly promising due to its relatively simple infrastructure requirements.[1] Then, optical functional devices that harness and convert sunlight have emerged as pivotal advancements in sustainable energy solutions. These devices utilize solar radiation and encompass technologies such as solar panels for electricity generation, solar-powered water evaporation systems,[2−4] photocatalytic materials for pollutant degradation, and photoelectrochemical cells for water splitting and other chemical reactions.[5−9] Integrating these devices into energy infrastructure enhances energy capture and conversion efficiency and promotes the adoption of solar energy technologies as a key component of renewable energy systems.

Two critical metrics determine the performance of optical devices: light absorbance and energy conversion efficiency. Light absorbance, the material's ability to capture photons across the solar spectrum, directly influences energy harvesting potential. Energy conversion efficiency quantifies the proportion of light converted into electricity (photovoltaic cells) or chemical energy (photocatalysis). Intrinsic material properties also play a decisive role in the device efficacy. Materials with low carrier recombination rates (prolonged electron−hole pair separation) excel in applications required high-efficiency charge transfer, such as electrodes for photoelectrochemical cells and photocatalysts.[10] Reduced recombination enables the more effective use of photogenerated charges for driving chemical reactions or generating electrical currents. Conversely, materials with higher recombination rates may be unsuitable for photovoltaic or photocatalytic applications due to premature carrier loss. However, these materials can be advantageous in solar-powered water evaporation systems, where maximizing photothermal conversion is prioritized over charge separation. Rapid carrier recombination in these systems contributes to localized heating, enhancing the photothermal effect and accelerating water evaporation.[11]

Carbon-based materials, including carbon foams, graphene, black phosphorus, and carbonized biomass (e.g., bamboo and sunflower stalks), have emerged as highly effective for solar water evaporation. Their broad light absorption and high thermal conductivity enhance water evaporation efficiency, making them suitable for water desalination, CO_2 reduction, and pollutant degradation.[12−15] They also contribute to environmental applications such as bacteria removal and soil remediation via solar vapor generation.[16,17] Integrating these materials into hybrid structures with metal oxides and sulfides further enhances their performance. For example, Cs_xWO_3-based fabrics achieve and evaporation efficiency of 86.8% and an evaporation rate of 1.34 kg·m^{-2}·h^{-1} under 1-Sun conditions.[18] Hierarchical CuS exhibits an even higher

Received: August 16, 2024
Revised: October 11, 2024
Accepted: October 15, 2024
Published: October 22, 2024

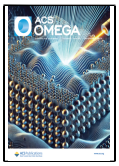

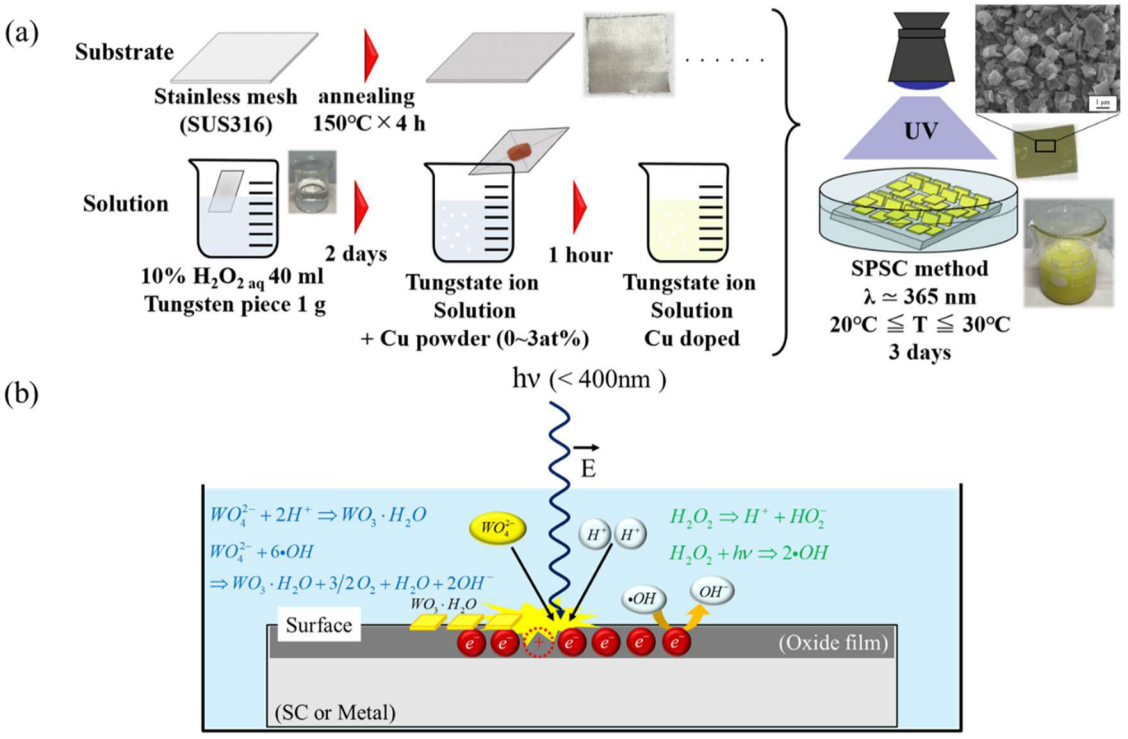

Figure 1. Schematic diagram of the one-pot SPsC process and its underlying mechanism. (a) Two-step preparation followed by the SPsC process. (b) Mechanism of the SPsC process for device fabrication.

evaporation efficiency (94.5% efficiency, 1.96 $kg{\cdot}m^{-2}{\cdot}h^{-1}$ evaporation rate), highlighting the potential of such hybrids.[19] Similarly, black phosphorus (88.66% efficiency, 1.35 $kg{\cdot}m^{-2}{\cdot}h^{-1}$ evaporation rate) demonstrates the effectiveness of two-dimensional materials for light absorption and heat localization.[20]

However, these materials face limitations that may affect their long-term viability in solar water evaporation systems. While more environmentally friendly than fossil fuels, the production and disposal of these materials can still pose environmental challenges, particularly when fabrication involves potentially polluting chemicals. Furthermore, the scalability for large-scale applications is hindered by fabrication complexity, cost, heat loss, and durability issues. Over time, these materials may degrade, reducing their effectiveness. Furthermore, their broad absorption spectrum, while generally beneficial, lacks the specificity of defined absorption peaks, potentially reducing efficiency in applications requiring precise energy conversion.[21]

Tungstic acid ($WO_3{\cdot}nH_2O$), an n-type semiconductor, is recognized for its superior light absorption capabilities and broad response wavelength spectrum, owing to its bandgap (E_g) ranging from 2.3 to 2.8 eV, which enables effective utilization of visible light (Vis) around 500 nm.[22] The crystal's performance is further enhanced by the introduction of dopants that induce structural defects, extending its responsiveness into the near-infrared (NIR) spectrum (800 to 2500 nm).[23] Specifically, copper (Cu) doping introduces oxygen vacancies (V_Os) within the $WO_3{\cdot}nH_2O$ structure, generating sub-bands in the bandgap that significantly enhance light absorption in the NIR region. A notable method for synthesizing $WO_3{\cdot}nH_2O$ is the submerged photosynthesis of crystallites (SPsC), which has proven to be an effective approach for creating unique nanostructures with remarkable optical properties.[23−26] The SPsC method not only enables the synthesis of $WO_3{\cdot}nH_2O$ but also facilitates the formation of heterostructures, allowing for the simultaneous production of nanocrystals and their direct integration onto substrates in a streamlined, one-pot fabrication process.[27−30] This method offers significant advantages over conventional techniques like spin coating and photolithography, which often introduce additional complexity and processing steps.[31−34] By operating under ambient conditions and utilizing only water and light as reactants, SPsC aligns with sustainable manufacturing practices, emphasizing process simplification, cost reduction, and minimal environmental impact.

In this study, we developed monohydrate tungstic acid ($WO_3{\cdot}H_2O$) nanoplates as an optical functional material and integrated them onto a stainless steel (SUS316) mesh, which is known for its exceptional chemical stability. The resulting composite device exhibited a uniform distribution of $WO_3{\cdot}H_2O$ nanoplates on the SUS316 mesh, significantly enhancing the optical properties compared to those of bare SUS316. Further improvements in these optical characteristics were achieved by doping the $WO_3{\cdot}H_2O$ nanoplates with Cu, enabling absorption across the entire solar spectrum. To evaluate the application performance of the Cu-doped $WO_3{\cdot}H_2O$ composite device, we conducted detailed examinations of its photothermal and photoelectrochemical conversion capabilities. During the photoelectrochemical tests, we observed variations in the cathodic current values and material conductivity under light illumination. These findings underscore the multifunctional potential of Cu-doped $WO_3{\cdot}H_2O$ nanoplates on SUS316 mesh, particularly in composite devices designed for photothermal, photoelectrochemical, and photoemission electron applications. The device's ability to convert solar energy into both thermal and electrical energy makes it

https://doi.org/10.1021/acsomega.4c07571
ACS Omega 2024, 9, 44714−44723

suitable for long-term, large-scale use in diverse environmental conditions.

2. MATERIALS AND METHODS

2.1. $WO_3{\cdot}H_2O$ Device Fabrication. The fabrication process is divided into two preparatory stages and the subsequent SPsC process (Figure 1a). The first stage involves preparation of the tungsten precursor. A tungsten foil measuring 0.10 × 200 × 200 mm^3 (99.95%, Nilaco, Japan) was immersed in a 10 wt % diluted hydrogen peroxide (H_2O_2) solution (Wako Pure Chemicals, Japan) and allowed to dissolve over approximately 2 days. Subsequently, Cu powder (99.8%, Nilaco, Japan) was introduced into the H_2O_2 solution at a copper-to-tungsten atomic ratio of 0−5%. This mixed solution was stirred for approximately 30 min until it turned clear yellow, indicating the formation of a homogeneous precursor solution. The second stage involves mesh preparation. SUS316 mesh (twilled tatami weave, 1000 MESH, Austenite Cr17% Ni12% Mo2.5%) was cut into 3 × 3 cm^2 segments. These mesh segments were then ultrasonically cleaned in ethanol for 5 min, followed by the same procedure using deionized water. After drying, the SUS316 mesh was placed in an alumina crucible and annealed at 150 °C for 4h in an electric furnace to remove surface impurities and promote the formation of a uniform oxide layer.

The final step is the one-pot SPsC process. The prepared solution is dispensed into an 18 cm^2 Petri dish, followed by immersion of the prepared SUS316 mesh into the solution. Subsequently, the setup is exposed to 66 mW/cm^2 ultraviolet (UV) light (λ = 365 nm, UVP B-100AP 100 W, Analytik Jena) while the solution is continuously stirred at a rate of 100 rpm. The UV irradiation is sustained for 72 h, during which the solution gradually transitions to a yellow and cloudy appearance, indicating the completion of the SPsC synthesis.

2.2. Surface and Structure Characterization. Surface morphology and elemental mapping were performed using a field emission type scanning electron microscopy (FE-SEM, JSM-7001FA, JEOL) equipped with energy-dispersive X-ray spectroscopy (EDX). The crystal structure was identified using X-ray diffraction (XRD, Rigaku Miniflex 600). XRD measurement was performed with Cu Kα line (λ = 1.5406 Å) and a scanning field of $3° \leq 2\theta \leq 90°$. Peak fitting was done in reference to JCPDS cards 00−052−0513 and 01−084−0886 for γ-Fe and $WO_3{\cdot}H_2O$, respectively. Cross sections of the sample device were prepared by using a cross-section polisher (CP, IB-09010CP, JEOL).

2.3. Investigation of Optical Properties of $WO_3{\cdot}H_2O$ Devices. The light absorption characteristics of the device were measured using a JASCO V-770 UV−vis−NIR spectrophotometer across a wavelength range of 200 to 2500 nm. The data obtained from this measurement are a fundamental quantity in optics termed wavelength-dependent absorbance ($A(\lambda)$), defined by eq 1

$$A(\lambda) = -\log\,(I/I_0) \tag{1}$$

Here, I_0 denotes the intensity of light incident on the sample and I represents the intensity of light transmitted through the sample. Absorbance, importantly, is a dimensionless quantity and therefore indicates the relative attenuation of light within the material. The absorption characteristics were evaluated and compared for each device with different amounts of Cu doping. To determine the device's E_g, we constructed a Tauc Plot using the acquired absorbance data. This analysis employed the following eq 2[35]

$$(\alpha h\nu)^{1/n} = A(h\nu - E_g) \tag{2}$$

where α is the absorption coefficient, h is Planck's constant, ν is the frequency of vibration, A is the proportional constant, n = 1/2 for direct semiconductor transitions, and n = 2 for indirect transitions. For $WO_3{\cdot}H_2O$ in this study, n = 2.

Then, the solar light utilization efficiency of the material was determined by integrating the product of the absorption coefficient and the solar spectral irradiance across the relevant wavelength range (λ_{min} to λ_{max}). This calculation is represented by eq 3

$$A_s(\lambda) = \frac{\int_{\lambda_{min}}^{\lambda_{max}} S(\lambda)\cdot[1 - R(\lambda) - T(\lambda)]\mathrm{d}\lambda}{\int_{\lambda_{min}}^{\lambda_{max}} S(\lambda)\mathrm{d}\lambda} \times 100\% \tag{3}$$

where A_s is solar absorbance. λ_{min} and λ_{max} denote the lower and upper wavelength limits of the integration, encompassing the relevant portion of the solar spectrum (300−1700 nm). $S(\lambda)$ signifies the solar spectra's irradiance, which represents the intensity of sunlight at a particular wavelength. It is noteworthy that eq 3 approximates the true solar light utilization efficiency. In a more comprehensive calculation, one would also consider the reflectance ($R(\lambda)$) and transmittance ($T(\lambda)$) of the material at each wavelength. For the sake of simplicity, we have incorporated the absorbance ($A(\lambda)$) and the solar spectra irradiance ($S(\lambda)$) as shown in eq 4

$$A_s(\lambda) = \frac{\int_{\lambda_{min}}^{\lambda_{max}} S(\lambda)\cdot[1 - \exp\,(-2.303A(\lambda))]\mathrm{d}\lambda}{\int_{\lambda_{min}}^{\lambda_{max}} S(\lambda)\mathrm{d}\lambda} \times 100\% \tag{4}$$

2.4. Photo Conversion Properties of the $WO_3{\cdot}H_2O$ Devices. We investigated the $WO_3{\cdot}H_2O$ device's energy conversion characteristics, focusing on photothermal, photoelectrochemical, and photoelectron emission properties.[8,36] To evaluate photothermal conversion, a solar water evaporation experiment was conducted using $WO_3{\cdot}H_2O$ nanoplates integrated on a 3 × 3 cm^2 SUS316 mesh. This device was placed in an 18 cm^2 Petri dish filled with 16 mL of deionized (DI) water, allowing sufficient space around the sample. To standardize the experimental conditions, the initial surface state of the $WO_3{\cdot}H_2O$ nanoplates (intermediate between hydrophobic and hydrophilic) was treated to ensure the device could float on the water surface during the experiment. Poly(dimethylsiloxane) (PDMS) dissolved in hexane at a concentration of 10 wt % was applied to the device's surface, followed by air drying for a few minutes, which imparted sufficient hydrophobicity to allow the samples to float freely on the water surface. Before initiating the photothermal measurements, the surface temperature of the device was recorded using infrared thermography (GTC400C Professional, BOSCH) to establish a baseline. The device was then irradiated with simulated sunlight (HAL-320W, Asahi Spectra Co., Ltd.) at an intensity of 100 mW/cm^2 (1 Sun) for 30 s, and the temperature changes were monitored. Additionally, to explore the utility of the NIR region, the device was irradiated with 500−1100 nm light (CWX150 × 03GM, Yazawa Co., Ltd.) at an intensity of 200 mW/cm^2, and the resulting temperature changes were recorded. These experiments were

https://doi.org/10.1021/acsomega.4c07571
ACS Omega 2024, 9, 44714−44723

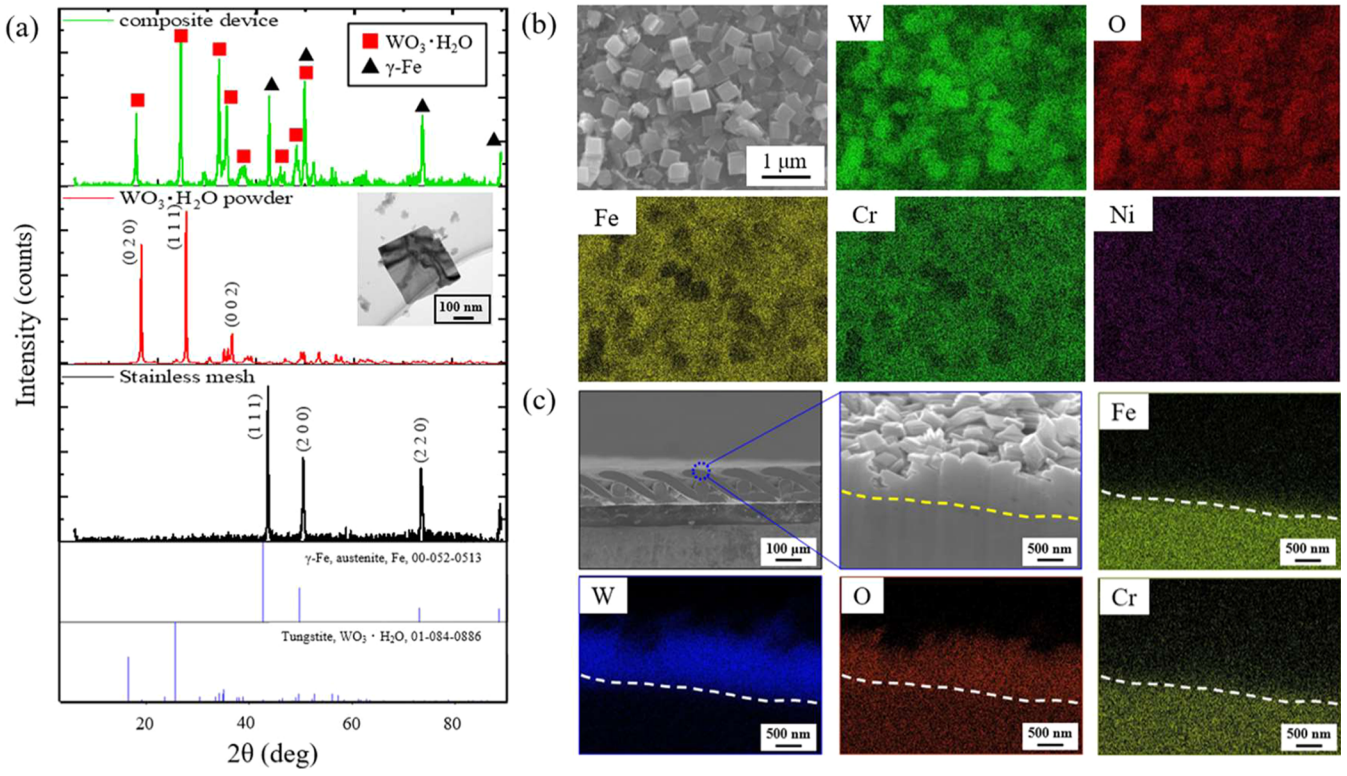

Figure 2. $WO_3{\cdot}H_2O$ device structural analysis. (a) XRD patterns of the SPsC-fabricated device. Inset TEM image shows a single $WO_3{\cdot}H_2O$ nanoplate. (b) SEM surface overview and corresponding EDX elemental mapping. (c) Cross-sectional SEM/EDX results.

conducted on both doped and undoped $WO_3{\cdot}H_2O$ devices for a comparative analysis.

For the evaluation of photoelectrochemical properties, cyclic voltammetry (CV) was employed using a three-electrode configuration.[37] The fabricated pure $WO_3{\cdot}H_2O$, as well as the Cu-doped $WO_3{\cdot}H_2O$ device served as the working electrode, with an Ag/AgCl/KCl (3 M) electrode (+0.208 V vs NHE at 25 °C) as the reference electrode, and a Pt wire (φ = 0.50 mm, purity 99.95%, Nilaco, Japan) as the counter electrode. A 0.5 M sulfuric acid solution (Wako Pure Chemical, Japan) was used as the electrolyte. The measurements were carried out using a potentiostat (PG302N, Metrohm Autolab) over a potential range of −0.7 V to +0.5 V, with sweep rates of 2, 3, 5, 10, 15, 20, and 50 mV/s. Experiments were conducted both with and without visible light irradiation (Xenon light source, 385−740 nm, 100 mW/cm^2, MAX-303, Asahi Spectra Co., Ltd.).

A photoelectron emission microscopy (PEEM) (My PEEM, SUGA Seisakujo) was used to directly observe photoelectron emissions.[38] During the measurement, UV light (λ = 365 nm) was focused near the boundary of these surfaces. An acceleration voltage of 5 kV was applied to observe the emitted photoelectrons. The relationship between the work function (eV) and the wavelength (nm) of the incident light is given by eq 5

$$E = h\nu = \frac{1240}{\lambda} = \frac{1}{2}mv^2 + W \tag{5}$$

While the fixed wavelength of this light source precludes direct work function determination, its high intensity facilitates the acquisition of clear observation images.

3. RESULTS AND DISCUSSION

3.1. Structural Analysis. Figure 2a presents the XRD patterns of the SPsC-fabricated $WO_3{\cdot}H_2O$ device, the $WO_3{\cdot}H_2O$ powder, and the SUS316 mesh. The SUS316 mesh exhibited only γ-Fe peaks, as the passive chromium and molybdenum oxide film on its surface is amorphous and nondiffracting. The $WO_3{\cdot}H_2O$ powder pattern solely revealed a peak corresponding to the monohydrate phase with no evidence of anhydrate, dihydrate, or other impurities. The SPsC-fabricated $WO_3{\cdot}H_2O$ device displayed peaks characteristic of both γ-Fe and tungstic acid, resembling the sum of the individual powder patterns (Figure 2a-red and black). Notably, doping with Cu resulted in a shift of the peaks toward lower angles by approximately 1° and broadening in the device's XRD pattern. These changes can be attributed to the ionic substitution of Cu^+ for W^{6+}, which necessitates charge compensation and leads to an expansion of the $WO_3{\cdot}H_2O$ lattice. The larger ionic radius of Cu^+ relative to W^{6+} (77 vs 60 pm) is responsible for this lattice expansion.[23]

Figure 2b summarizes the SEM image and EDX mapping of the SPsC-fabricated $WO_3{\cdot}H_2O$ device. In contrast to the smooth surface of the raw SUS316 mesh, the SEM image revealed uniformly integrated $WO_3{\cdot}H_2O$ nanoplates (Figure S1). EDX mapping confirmed the presence of W and O, with their elemental distributions being consistent with the crystal morphology. Combined with the XRD and transmission electron microscopy (TEM) results (Figure S2), these findings confirm the crystal to be $WO_3{\cdot}H_2O$. In regions with minimal crystal migration, elements like Fe, Cr, and Ni, originating from the SUS316 mesh, were detected. Notably, the Cr content exceeded the expected mesh's nominal composition, suggesting the accrual of a chromium oxide film atop the mesh surface. Interestingly, the fabricated nanoplates exhibited

https://doi.org/10.1021/acsomega.4c07571
ACS Omega 2024, 9, 44714−44723

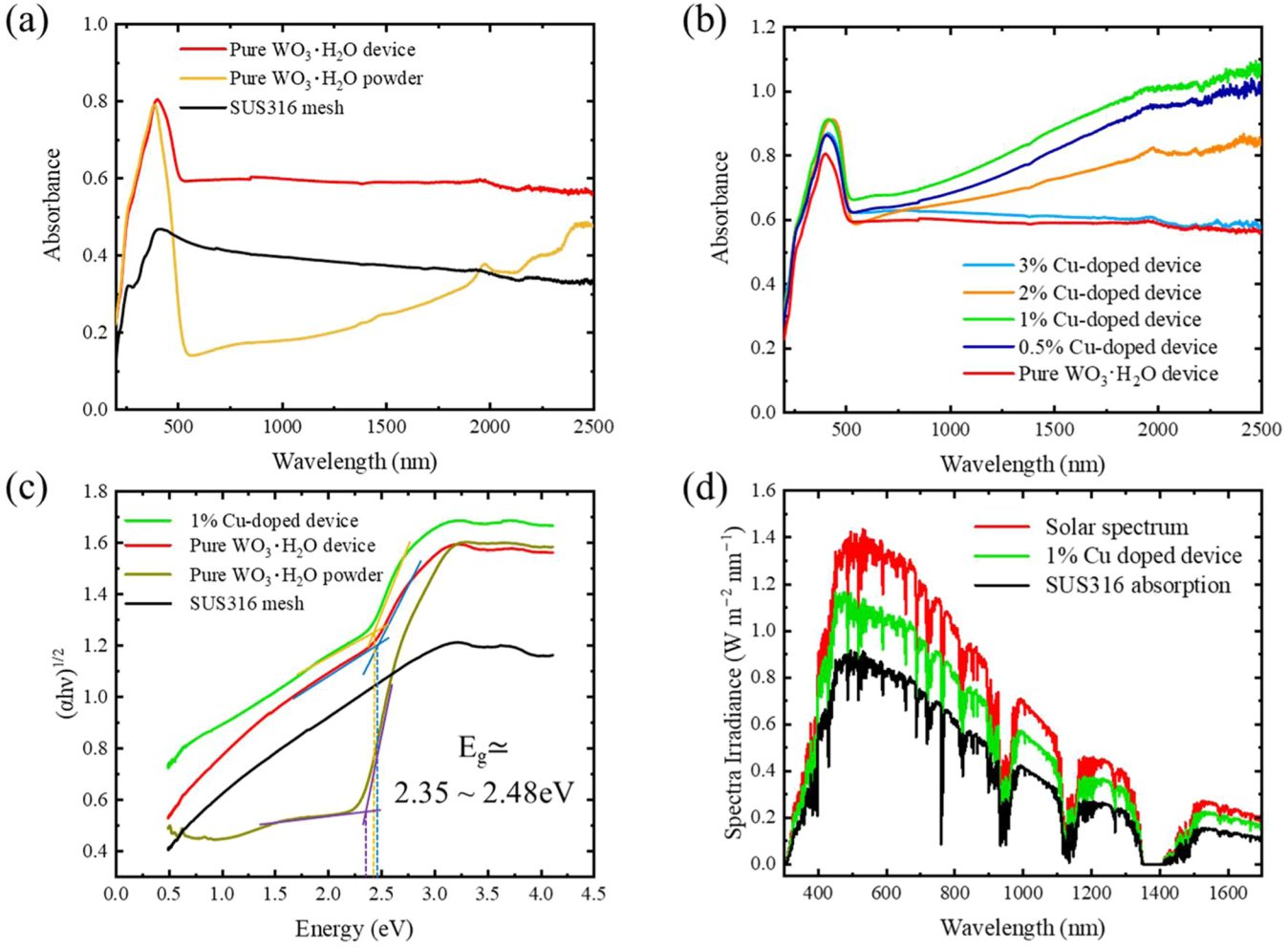

Figure 3. Optical properties of the $WO_3{\cdot}H_2O$ device. (a) Comparative UV−Vis−NIR absorbance spectra of the SUS316 mesh, pure $WO_3{\cdot}H_2O$ powder, and the SPsC-fabricated pure $WO_3{\cdot}H_2O$ device. (b) UV−vis−NIR absorbance spectra for devices based on pure $WO_3{\cdot}H_2O$ and those doped with 0.5−3% Cu. (c) Tauc plot for E_g estimation for the SUS316 mesh, pure $WO_3{\cdot}H_2O$ powder, pure $WO_3{\cdot}H_2O$ device, and 1% Cu-doped $WO_3{\cdot}H_2O$ device. (d) Solar spectra irradiance for the SUS316 mesh, the 1% Cu-doped $WO_3{\cdot}H_2O$ device, compared with the solar spectrum.

uniform coverage across the surface, extending even to the backside, which was not directly exposed to light during synthesis. This suggests that crystal nucleation and growth may be influenced by factors beyond direct light exposure. Potential factors include solution diffusion, differences in surface energy, heat transfer through the mesh, scattered or reflected light, and the migration of reactive species such as hydroxyl radicals ($^{\bullet}OH$).[23,24]

Figure 2c presents the cross-sectional SEM and EDX observations of the device. As is evident in the middle SEM image, the $WO_3{\cdot}H_2O$ nanoplates are densely stacked to the SU316 mesh surface. The nanoplates exhibit uniform layering throughout and a thickness of approximately 1.2−1.3 μm as corroborated by the W distribution in the EDX map. The thickness corresponds to a layering of about 15 to 20 square nanoplates stacked atop one another. This finding confirms the successful integration of $WO_3{\cdot}H_2O$ on the SUS316 mesh achieved through a one-pot SPsC synthesis. By controlling the synthesis conditions, including solute concentrations and UV irradiation, it is feasible to adjust the stacking density and thickness of the nanoplates layers.

Figure 1b summarizes the growth reaction mechanisms of the one-pot SPsC. In the initial crystal formation stage, when H_2O_2 is irradiated with UV light with a wavelength of 400 nm or less, active species of $^{\bullet}OH$ are generated in the solution (eq 6).

$$H_2O_2 + h\nu \rightarrow 2{\cdot}OH \tag{6}$$

This radical generation reaction is wavelength dependent. It does not occur upon irradiation with lower-energy visible light, leading to distinct final products compared with those formed under UV excitation. Subsequently, dissolved tungstic acid ions (WO_4^{2-}) react with the generated $^{\bullet}OH$ to yield $WO_3{\cdot}H_2O$, as described by eq 7

$$2WO_4^{2-} + 4{\cdot}OH + 2H_2O \rightarrow 2WO_3{\cdot}H_2O + O_2 + 4OH^- \tag{7}$$

We propose that UV irradiation induces an electric field effect within the solution, leading to preferential alignment of anions and cations.[23,37] This alignment results in directional collisions and contributes to the formation of the observed planar crystals. Furthermore, eq 7 indicates the consumption of hydrogen ions, implying a pH increase, which was experimentally confirmed (ΔpH $\approx$ 0.3). We theorize that increasing the tungsten concentration or reaction time could amplify this pH change, thereby influencing the crystal growth kinetics. Regarding the stacking mechanism, UV irradiation on the SUS316 generates electrons via the photoelectric effect,

https://doi.org/10.1021/acsomega.4c07571
ACS Omega 2024, 9, 44714−44723

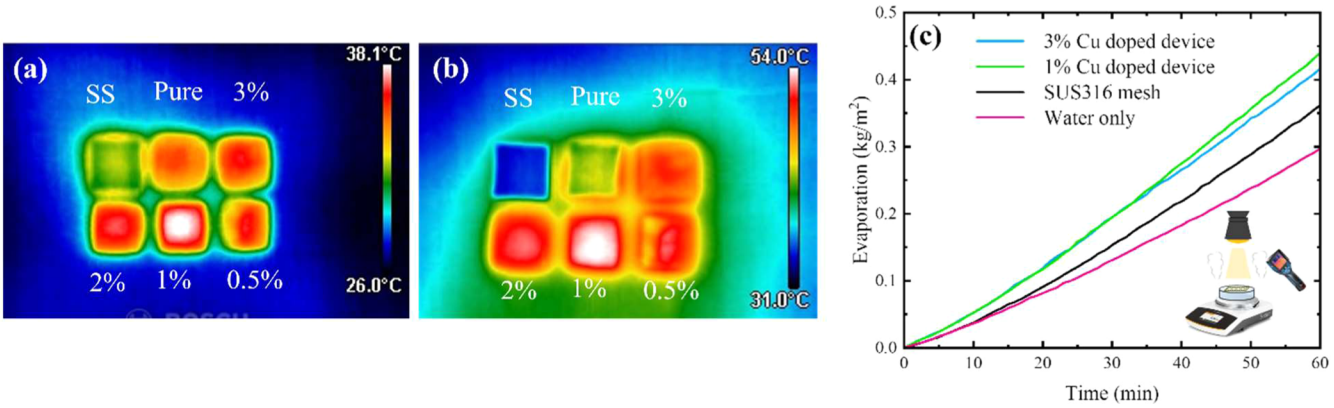

Figure 4. Photothermal conversion properties of the $WO_3 \cdot H_2O$ device. (a) Photothermal image under simulated sunlight (1-Sun) irradiation. (b) Photothermal image under NIR light irradiation. (c) Solar water evaporation graph, comparing water, the SUS316 mesh, and 1−3% Cu-doped $WO_3 \cdot H_2O$ devices.

primarily within the chromium oxide film. This film's bandgap (2.4−3.5 eV)[39,40] corresponds to the energy of the utilized UV light. $^{\bullet}OH$ in the solution scavenges some of these electrons, creating localized electron-deficient regions on the mesh surface. Attracted to these regions, negatively charged tungstate ions preferentially react, in principle, as shown in eq 7, establishing crystal deposition sites. Concurrently, the acidic solution likely leads to a continuous cycle of dissolution and reprecipitation of the SUS316's oxide film, potentially enhancing the crystal-SUS316 bonding.

3.2. Optical Properties Analysis. Figure 3a presents the absorbance spectra of the SPsC-fabricated device, the $WO_3 \cdot H_2O$ powder, and the SUS316 mesh. The device's spectrum closely resembles the sum of the individual spectra, exhibiting high absorbance across the entire wavelength range. Notably, the absorbance remains above 0.6 at wavelengths exceeding 600 nm, translating to an estimated absorbance increase of approximately 75%.[41] This indicates excellent light absorption characteristics for the device. The peak observed around 500 nm in the spectra of both the crystal and the device corresponds to the E_g of $WO_3 \cdot H_2O$. The peak near 2000 nm is attributed to water absorption within the interlayer structure.

Figure 3b reveals the significant impact of 0−3% Cu doping on the absorbance of the devices. Only the device doped with 3% Cu exhibited an absorbance comparable to that of pure (0% Cu) $WO_3 \cdot H_2O$. For all other doping concentrations, a notable increase in absorbance was observed, particularly in the NIR region. The 1% Cu-doped device displayed the highest absorbance, reaching a value close to 1.1, which corresponded to an absorbance increase of approximately 92%. We attribute this improvement to the structural and electronic modifications induced by Cu doping. At lower doping levels, Cu likely substitutes for W within the $WO_3 \cdot H_2O$ lattice, creating V_Os. These V_Os, in combination with structural distortions caused by Cu incorporation, elevate the valence band maximum, reduce the E_g, and introduce sub-bands within the gap.[23] The resulting band structure facilitates enhanced absorption, especially in the low-energy infrared region.

The 1% Cu doping appears to represent an opto-critical state, where an optimal balance is manifested between V_O concentration and $WO_3 \cdot H_2O$ lattice integrity.[23] Higher Cu concentrations (2 and 3%) might lead to excessive lattice distortion and V_O annihilation, hindering sub-band formation and reducing infrared absorption.[23] Figure 3c displays the Tauc plots for selected samples. By extrapolating tangents to the steepest linear regions, we estimate E_g values within the expected range of 2.35 to 2.48 eV. Consistent with our discussion, the 1% Cu-doped device exhibits an approximately 0.04 eV smaller E_g than the undoped device. This reduction is mainly attributed to the introduction of defect states within the bandgap due to Cu doping. Interestingly, while the Cu-doped $WO_3 \cdot H_2O$ powder exhibits an even lower E_g, the Cu-doped $WO_3 \cdot H_2O$ device displays a slightly larger bandgap compared to their powder counterpart. Several potential factors could contribute to this difference: first, the confined growth environment within the mesh might include lattice strains or altered defect distributions in Cu-doped $WO_3 \cdot H_2O$ compared to the freely formed powder, thereby influencing the E_g. Second, minor interdiffusion from the SUS316, particularly chromium, into $WO_3 \cdot H_2O$ is plausible. These diffusing species could introduce additional defect states, subtly affecting the E_g.

Figure 3d presents the solar absorption spectra of the selected samples. The red line represents the reference spectrum of sunlight reaching the Earth's surface at various wavelengths. The black and green lines depict the results of integrating the absorbance data from Figures 3a,b into eq 4. The absorbance, calculated by comparing the areas under the green and black curves to the area under the red curve, is 60.42% for the bare SUS316 mesh and 81.40% for the 1% Cu-doped device. This enhanced ability to absorb infrared light allows the device to maintain a high absorbance across a broader wavelength range. Consequently, this device holds promise for excellent performance in various solar energy conversion applications.

3.3. Photothermal Conversion Properties. Upon light absorption, semiconductors such as WO_3 generate electron−hole pairs (excitons), which can dissociate to contribute to current flow, participate in chemical reactions, or undergo recombination. The nature of exciton recombination is crucial for determining the device's energy conversion pathways. In $WO_3 \cdot H_2O$, minimal radiative recombination under illumination suggests a strong propensity for nonradiative pathways, leading to the conversion of light energy into heat—a key mechanism for photothermal conversion. When Cu is doped into $WO_3 \cdot H_2O$, the introduction of V_O and Cu-induced midgap states increases the likelihood of nonradiative recombination, effectively enhancing the device's photothermal conversion efficiency. This process is beneficial for applications

https://doi.org/10.1021/acsomega.4c07571
ACS Omega 2024, 9, 44714−44723

such as solar water evaporation, where the primary goal is to maximize heat generation from absorbed light.

Figure 4a presents the surface temperature increase upon simulated sunlight irradiation for each SPsC-fabricated device. Initially, all devices exhibited a surface temperature of approximately 25−26 °C, close to room temperature. SUS316 displayed the smallest temperature increase (around 30 °C), while the 1% Cu-doped device achieved the highest temperature (38 °C). This aligns well with the previously observed superior solar utilization efficiency of the 1% Cu-doped device.[23] The significant temperature increase in the Cu-doped device suggests a high recombination rate for photoexcited electrons and holes within the sub-bands created by infrared light absorption. This high recombination rate, attributed to the reduced E_g in these sub-bands,[42] leads to efficient thermal energy transfer.

Figure 4b depicts a similar experiment using NIR light (≈900 nm) irradiation. The temperature increase trend mirrored that observed under 1-Sun. The SUS316 mesh exhibited the lowest temperature increase (31 °C), whereas the 1% Cu-doped device reached the highest temperature (54 °C). These results confirm the device's ability to effectively utilize light across the visible and NIR regions, wavelengths typically challenging for conventional materials. Furthermore, they support the hypothesis that a significant portion of the NIR light absorbed by the sub-bands undergoes recombination and subsequent conversion into heat. Figure 4c summarizes the water evaporation changes over a 60 min solar water evaporation experiment conducted under the same conditions as Figure 4a. Table 1 details the evaporation rate and surface temperature of each device derived from this experiment.

Table 1. Water Evaporation Rate and Sample Photothermal Surface Temperature during the Solar Water Evaporation Experiment

sample	water evaporation rate ($kg·m^{-2}·h^{-1}$)	photothermal surface temperature (°C)
3% Cu-doped $WO_3·H_2O$ device	0.416	34.4
1% Cu-doped $WO_3·H_2O$ device	0.440	37.2
SUS316 mesh	0.362	31.6
water	0.297	31.2

The 1% Cu-doped device consistently exhibited the highest performance in this experiment. Using eq 8,[3,43] we calculated the energy conversion efficiency η

$$\eta = \frac{m_t h_\nu(T)}{1000 C_{opt}} \tag{8}$$

where m_t (kg m^{-2} h^{-1}) is the evaporation rate, $h_\nu(T)$ is the evaporation enthalpy of water, and C_{opt} is the solar concentration. Substituting the data for the 1% Cu-doped $WO_3·H_2O$ device yielded an energy conversion efficiency of 32.5%. While this value is lower than anticipated, we attribute the difference to energy consumed in heating the water. Since the material exhibits photothermal conversion, a portion of the absorbed energy raises the water temperature before evaporation can occur. This implies that the long-term operation of the system could lead to progressively higher efficiency. Importantly, there is negligible deterioration even after 2 h of continuous operation, confirming the device's durability.

We believe that the evaporation rates reported here do not represent the inherent limits of these devices. Although the Cu-doped $WO_3·H_2O$ nanoplates exhibit a relatively lower water evaporation rate of 0.440 $kg·m^{-2}·h^{-1}$ under standard 1-Sun condition, they offer several key advantages that make them highly valuable for long-term and large-scale applications. The device achieves an energy conversion efficiency of 32.5%, which, while modest, is bolstered by its unique ability to absorb a broad range of the solar spectrum, including distinct visible light absorption at 600 nm (Figure 3b) and increased NIR absorption due to the V_Os. This enhanced absorption is attributed to the presence of five-coordinated W atoms in local defect regions, which create localized electronic states that facilitate broader solar absorption, particularly in the visible and NIR regions. Additionally, the structural role of water molecules within the $WO_3·H_2O$ framework can act as a buffering system, providing stability and durability against extremely acidic and alkaline conditions. This combination of enhanced photothermal properties and robust chemical stability sets $WO_3·H_2O$ apart from many other materials, particularly in challenging environments, such as seawater desalination, where other materials might degrade over time.

Previous research indicates that adjustments to environmental conditions, such as controlled convection, radiation, and device configuration, can potentially double the evaporation efficiency.[4,44−46] This suggests promising avenues for further optimizing the performance of our device. Beyond solar evaporation, the material demonstrates potential for pollutant and bacteria decomposition in raw water due to its photocatalytic properties,[47,48] underscoring the device's multifunctional capabilities.

3.4. Photochemical and Photoelectron Conversion Properties. Figure 5 presents CV measurements of a 1% Cu-doped device as the working electrode. The blue line represents data acquired under dark conditions, while the red line corresponds to data obtained under light illumination. The gray line depicts measurements on bare SUS316 mesh for

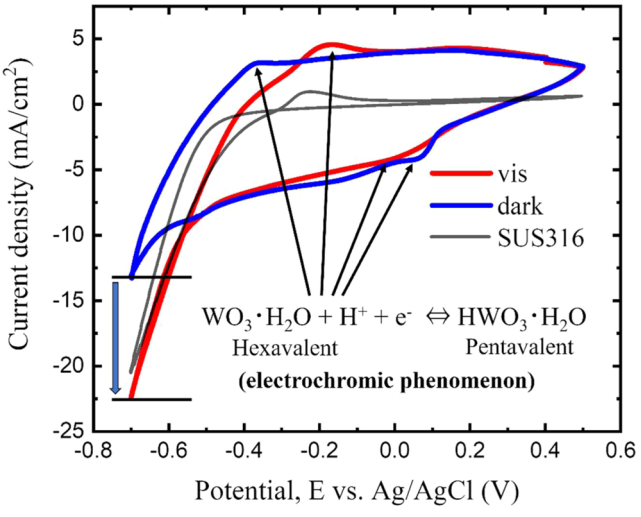

Figure 5. Photoelectrochemical performance test by CV for the 1% Cu-doped $WO_3·H_2O$ device under visible light illumination, compared with dark conditions (no illumination) and the SUS316 mesh.

https://doi.org/10.1021/acsomega.4c07571
ACS Omega 2024, 9, 44714−44723

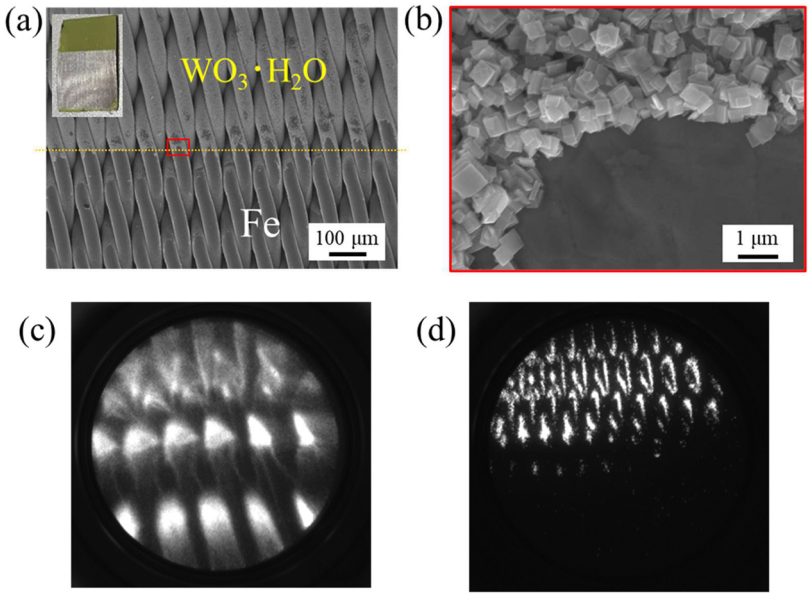

Figure 6. PEEM observation results of the 1% Cu-doped $WO_3 \cdot H_2O$ device. (a) SEM image of the target PEEM measurement area. The inset shows an optical image of the device. The metallic surface is attributed to the bare SUS316 surface after the Kapton tape is removed. The orange line indicates the interface between the Cu-doped $WO_3 \cdot H_2O$ nanoplates and the bare SUS316 surface. (b) Magnified SEM view of the interface, taken from the red squared area in (a). (c, d) PEEM images with and without the effect of scattered light, respectively.

comparison purposes. All CV scans were performed at a sweep rate of 3 mV/s. Other sweep rates (Figure S4) reveal a consistent trend where the magnitude of the current density increases with the sweep rates under both dark and illuminated conditions. This observed increase in the current density during the CV experiments is intricately linked to the incorporation of Cu into the $WO_3 \cdot H_2O$ lattice. The Cu doping introduces additional electronic states within $WO_3 \cdot H_2O$, which enhances the number of available charge carriers, primarily electrons. These additional carriers contribute to the observed rise in current density, particularly as the potential is dynamically swept across a range during the CV measurements. This is a critical point to emphasize, as the CV experiment inherently involves a varying potential, which distinguishes it from measurements conducted at a constant potential.

Three key observations can be drawn from the CV data upon light irradiation. First, the redox peak in the illuminated device (red line) exhibits a negative shift compared to the dark condition (blue line), which is indicative of an increase in electron carrier density on the sample surface. This increase is particularly due to the introduction of Cu into the $WO_3 \cdot H_2O$ lattice, which, as discussed earlier, creates additional electronic states that boost the overall carrier density. The dynamic nature of the potential sweep during the CV experiment further accentuates this effect, as the continuous variation in the potential enables a broader engagement of these carriers in the redox reactions.

Second, the cathodic current density at −0.7 V significantly increases under light irradiation, rising from 13.2 mA/cm^2 in the dark to 22.5 mA/cm^2 under illumination (1.7-fold increase). This enhancement is again attributed to the rise in electron carrier concentration induced by light. As the number of mobile electrons increases, a higher current is measured at a constant applied potential. Finally, the capacitance of the device, estimated from the CV curve's integrated area, decreases upon light irradiation. The capacitance under the dark condition is 1.08 F/cm^2, whereas it reduces to 0.871 F under illumination (a decrease of approximately 20%). This change suggests a light-induced transition from capacitive to conductive behavior, particularly on the cathode side. Notably, the red curve (illuminated device) in the cathodic region closely resembles the gray curve (SUS316 mesh), implying that the illuminated device exhibits conductor-like behavior in this regime. For photoelectrochemical applications, efficient charge carrier separation and transport are critical. Our previous studies have demonstrated that Cu doping induces a semiconductor-to-metal transition,[23] enhancing the device's conductivity and charge carrier mobility. This transition reduces recombination, allowing more charge carriers to reach the electrode interface and participate in electrochemical reactions.

In the dark condition, the device's conduction band likely lies below the hydrogen evolution potential (indicated by the −0.7 V peak). Consequently, electrons are unlikely to participate directly in hydrogen generation. However, light irradiation elevates the Fermi level due to the increased electron concentration, shifting the entire band structure toward higher energy levels. This shift positions the conduction band above the hydrogen evolution potential, enabling excited electrons to readily contribute to hydrogen evolution and resulting in the observed increase in current. This unique light-modulated capacitive and conductive behavior makes this device a promising candidate for various applications including sensors and rectifying diodes.

Figure 6 presents the PEEM measurement results of the 1% Cu-doped $WO_3 \cdot H_2O$ device surface. To facilitate this measurement, Kapton tape was used during SPsC to retain a bare SUS316 surface, as shown in the optical image inset (Figure 6a). Figure 6a,b exhibits the interface where the SUS316 and Cu-doped $WO_3 \cdot H_2O$ nanoplates meet. Figure 6c,d shows the PEEM images of the identical region. Figure 6c incorporates the effect of scattered light, while Figure 6d is devoid of such light, offering a PEEM signal obtained solely

https://doi.org/10.1021/acsomega.4c07571
ACS Omega 2024, 9, 44714−44723

from the $WO_3 \cdot H_2O$. Both images display a brighter upper half corresponding to the exposed $WO_3 \cdot H_2O$ surface, providing direct evidence of photoelectron emission. Although the current experiment did not allow for precise work function determination, it is important to emphasize the significance of this measurement. Future studies employing a deuterium lamp with a tunable wavelength source can accurately measure the work function, thereby providing more detailed insights into the electronic properties of the $WO_3 \cdot H_2O$ surface.

4. CONCLUSIONS

In this work, we successfully developed and demonstrated a one-pot fabrication approach, the SPsC method, for the direct formation of $WO_3 \cdot H_2O$ nanoplates on an SUS316 mesh. The fabricated $WO_3 \cdot H_2O$ devices exhibited a broadband absorbance across the UV−vis−NIR spectrum. Notably, the 1% Cu-doped device maintained remarkably high absorbance in the NIR region, achieving a solar utilization efficiency of 81.40%. Additionally, the device displayed distinctive photothermal and photoelectric conversion properties, suggesting the potential for diverse applications. Our findings establish the effectiveness of the SPsC method in producing high-performance optical functional devices. Crucially, this method offers an environmentally friendly alternative for the fabrication of other nanodevices.

■ ASSOCIATED CONTENT

Supporting Information

The Supporting Information is available free of charge at https://pubs.acs.org/doi/10.1021/acsomega.4c07571.

Additional SEM images of pure $WO_3 \cdot H_2O$ fabricated device; TEM image and SAED pattern of the $WO_3 \cdot H_2O$ nanoplate; water evaporation under NIR light irradiation; and CV curves under different sweep rates (PDF)

■ AUTHOR INFORMATION

Corresponding Author

Seiichi Watanabe − *Faculty of Engineering, Hokkaido University, Sapporo 060-8628, Japan;* orcid.org/0000-0002-4843-7493; Email: sw004@eng.hokudai.ac.jp

Authors

Mahiro Nishimura − *Graduate School of Engineering, Hokkaido University, Sapporo 060-8628, Japan*

Hiroto Miyashita − *Graduate School of Engineering, Hokkaido University, Sapporo 060-8628, Japan*

Hsueh-I Lin − *Graduate School of Engineering, Hokkaido University, Sapporo 060-8628, Japan*

Lihua Zhang − *Faculty of Engineering, Hokkaido University, Sapporo 060-8628, Japan*

Melbert Jeem − *Faculty of Engineering, Hokkaido University, Sapporo 060-8628, Japan;* orcid.org/0000-0002-6911-436X

Complete contact information is available at: https://pubs.acs.org/10.1021/acsomega.4c07571

Author Contributions

M.N.: investigation, data curation, formal analysis, writing—original draft. H.M.: investigation, data curation, formal analysis, validation; H.-I.L.: investigation, data curation, formal analysis, validation; L.Z.: validation, funding acquisition; M.J.; writing—review and editing; S.W.: supervision, conceptualization, methodology, validation, funding acquisition.

Notes

The authors declare no competing financial interest.

■ ACKNOWLEDGMENTS

The authors thank Mr. Kenji Ohkubo for his assistance with the PEEM measurement. This work was financially supported by the Japan Society for the Promotion of Science (grant no: JP21K04823, JP20H00295). The work was conducted at Hokkaido University, supported by "Advanced Research Infrastructure for Materials and Nanotechnology in Japan (ARIM)" of the Ministry of Education, Culture, Sports, Science and Technology (MEXT).

■ REFERENCES

(1) Ibrahim, I.; Seo, D. H.; McDonagh, A. M.; Shon, H. K.; Tijing, L. Semiconductor photothermal materials enabling efficient solar steam generation toward desalination and wastewater treatment. *Desalination* **2021**, *500*, No. 114853.

(2) Chang, C.; Yang, C.; Liu, Y.; Tao, P.; Song, C.; Shang, W.; Wu, J.; Deng, T. Efficient Solar-Thermal Energy Harvest Driven by Interfacial Plasmonic Heating-Assisted Evaporation. *ACS Appl. Mater. Interfaces* **2016**, *8*, 23412−23418.

(3) Li, S.; Xi, Z.; Yu, L.; Yan, H.; Chen, M. Thermal Management of the Solar Evaporation Process. *Langmuir* **2023**, *39*, 8900−8907.

(4) Xu, Y.; Ma, J.; Han, Y.; Zhang, J.; Cui, F.; Zhao, Y.; Li, X.; Wang, W. Multifunctional CuO Nanowire Mesh for Highly Efficient Solar Evaporation and Water Purification. *ACS Sustainable Chem. Eng.* **2019**, *7*, 5476−5485.

(5) Liao, Y.; Zhang, H.; Zhong, Z.; Jia, L.; Bai, F.; Li, J.; Zhong, P.; Chen, H.; Zhang, J. Enhanced Visible-Photocatalytic Activity of Anodic TiO_2 Nanotubes Film via Decoration with $CuInSe_2$ Nanocrystals. *ACS Appl. Mater. Interfaces* **2013**, *5*, 11022−11028.

(6) Douglas, J. J.; Sevrin, M. J.; Stephenson, C. R. J. Visible Light Photocatalysis: Applications and New Disconnections in the Synthesis of Pharmaceutical Agents. *Org. Process Res. Dev.* **2016**, *20*, 1134−1147.

(7) Bhoyate, S.; Kahol, P. K.; Gupta, R. K. Broadening the Horizon for Supercapacitor Research via 2D Material Systems. In *Nanoscience*; Revaprasadu, N., Ed.; The Royal Society of Chemistry, 2020; Vol. *6*, pp 120−149.

(8) Li, W.; Da, P.; Zhang, Y.; Wang, Y.; Lin, X.; Gong, X.; Zheng, G. WO_3 Nanoflakes for Enhanced Photoelectrochemical Conversion. *ACS Nano* **2014**, *8*, 11770−11777.

(9) Gahlawat, S.; Singh, J.; Yadav, A. K.; Ingole, P. P. Exploring Burstein−Moss Type Effects in Nickel Doped Hematite Dendrite Nanostructures for Enhanced Photo-Electrochemical Water Splitting. *Phys. Chem. Chem. Phys.* **2019**, *21*, 20463−20477.

(10) Panayotov, D. A.; Morris, J. R. Surface chemistry of Au/TiO_2: Thermally and photolytically activated reactions. *Surf. Sci. Rep.* **2016**, *71*, 77−271.

(11) Sun, Z.; Huang, F.; Cai, Y.; Liang, W.; Fan, S.; Tu, C.; Liu, Y.; Yan, C. A flexible sanded cotton fabric coated with Au@polypyrrole for seawater desalination. *Chem. Eng. J.* **2024**, *492*, No. 152309.

(12) Djellabi, R.; Noureen, L.; Dao, V.-D.; Meroni, D.; Falletta, E.; Dionysiou, D. D.; Bianchi, C. L. Recent advances and challenges of emerging solar-driven steam and the contribution of photocatalytic effect. *Chem. Eng. J.* **2022**, *431*, No. 134024.

(13) Liu, H.; Ye, H.-G.; Gao, M.; Li, Q.; Liu, Z.; Xie, A.-Q.; Zhu, L.; Ho, G. W.; Chen, S. Conformal Microfluidic-Blow-Spun 3D Photothermal Catalytic Spherical Evaporator for Omnidirectional Enhanced Solar Steam Generation and CO_2 Reduction. *Adv. Sci.* **2021**, *8*, No. 2101232.

(14) Chen, R.; Zhang, T.; Kim, J.; Peng, H.; Ye, M.; Huang, C.-H. Interfacial Solar Distillation for Freshwater Production: Fate of

Volatile and Semivolatile Organic Contaminants. *Environ. Sci. Technol.* **2021**, *55*, 6248−6256.
(15) Fan, D.; Lu, Y.; Zhang, H.; Xu, H.; Lu, C.; Tang, Y.; Yang, X. Synergy of photocatalysis and photothermal effect in integrated 0D perovskite oxide/2D MXene heterostructures for simultaneous water purification and solar steam generation. *Appl. Catal., B* **2021**, *295*, No. 120285.
(16) Peng, B.; Gao, Y.; Lyu, Q.; Xie, Z.; Li, M.; Zhang, L.; Zhu, J. Cationic Photothermal Hydrogels with Bacteria-Inhibiting Capability for Freshwater Production via Solar-Driven Steam Generation. *ACS Appl. Mater. Interfaces* **2021**, *13*, 37724−37733.
(17) Wu, P.; Wu, X.; Xu, H.; Owens, G. Interfacial solar evaporation driven lead removal from a contaminated soil. *EcoMat* **2021**, *3*, No. e12140.
(18) Gao, X.; Lan, H.; Li, S.; Lu, X.; Zeng, M.; Gao, X.; Wang, Q.; Zhou, G.; Liu, J.-M.; Naughton, M. J.; Kempa, K.; Gao, J. Artificial Mushroom Sponge Structure for Highly Efficient and Inexpensive Cold-Water Steam Generation. *Global Challenges* **2018**, *2*, No. 1800035.
(19) Tyagi, H.; Phelan, P.; Prasher, R. Predicted Efficiency of a Low-Temperature Nanofluid-Based Direct Absorption Solar Collector. *J. Sol. Energy Eng.* **2009**, *131*, No. 041004, DOI: 10.1115/1.3197562.
(20) Kong, Y.; Dan, H.; Kong, W.; Gao, Y.; Shang, Y.; Ji, K.; Yue, Q.; Gao, B. Self-floating maize straw/graphene aerogel synthesis based on microbubble and ice crystal templates for efficient solar-driven interfacial water evaporation. *J. Mater. Chem. A* **2020**, *8*, 24734−24742.
(21) Dao, V.-D.; Vu, N. H.; Yun, S. Recent advances and challenges for solar-driven water evaporation system toward applications. *Nano Energy* **2020**, *68*, No. 104324.
(22) Suzuki, H.; Tomita, O.; Higashi, M.; Abe, R. Tungstic Acids H_2WO_4 and H_4WO_5 as Stable Photocatalysts for Water Oxidation Under Visible Light. *J. Mater. Chem. A* **2017**, *5*, 10280−10288.
(23) Jeem, M.; Hayano, A.; Miyashita, H.; Nishimura, M.; Fukuroi, K.; Lin, H.-I.; Zhang, L.; Watanabe, S. Defect Driven Opto-Critical Phases Tuned for All-Solar Utilization. *Adv. Mater.* **2023**, *35*, No. 2305494.
(24) Jeem, M.; Bin Julaihi, M. R. M.; Ishioka, J.; Yatsu, S.; Okamoto, K.; Shibayama, T.; Iwasaki, T.; Kato, T.; Watanabe, S. A Pathway of Nanocrystallite Fabrication by Photo-Assisted Growth in Pure Water. *Sci. Rep.* **2015**, *5*, No. 11429.
(25) Jeem, M.; Zhang, L.; Ishioka, J.; Shibayama, T.; Iwasaki, T.; Kato, T.; Watanabe, S. Tuning Optoelectrical Properties of ZnO Nanorods with Excitonic Defects via Submerged Illumination. *Nano Lett.* **2017**, *17*, 2088−2093.
(26) Zhang, L.; Jeem, M.; Okamoto, K.; Watanabe, S. Photochemistry and the Role of Light during the Submerged Photosynthesis of Zinc Oxide Nanorods. *Sci. Rep.* **2018**, *8*, No. 177.
(27) Takahashi, Y.; Hiraiwa, K.; Jeem, M.; Zhang, L.; Watanabe, S. Galvanic-Submerged Photosynthesis of Crystallites: Fabrication of ZnO Nanorods@Cu-Surface. *Appl. Surf. Sci.* **2019**, *489*, 313−320.
(28) Hiraiwa, K.; Takahashi, Y.; Mizuno, J.; Jeem, M.; Watanabe, S. Luminescence Properties of ZnO-M Heterostructures Fabricated by Galvanic-Submerged Photosynthesis of Crystallites. *Appl. Surf. Sci.* **2019**, *489*, 269−277.
(29) Takahashi, Y.; Jeem, M.; Zhang, L.; Watanabe, S. The Origin of Opto-Functional Enhancement in ZnO/CuO Nanoforest Structure Fabricated by Submerged Photosynthesis. *Appl. Mater. Today* **2022**, *26*, No. 101359.
(30) Mizuno, J.; Jeem, M.; Takahashi, Y.; Kawamoto, M.; Asakura, K.; Watanabe, S. Light and Shadow Effects in the Submerged Photolytic Synthesis of Micropatterned CuO Nanoflowers and ZnO Nanorods as Optoelectronic Surfaces. *ACS Appl. Nano Mater.* **2020**, *3*, 1783−1791.
(31) Yun, J.; Kim, J.; Yang, M.; Kang, B. Low-Cost Laser Printable Photomask: One-Step, Photoresist-Free, Fully Solution Processed High-Grade Photolithography Mask. *Appl. Surf. Sci.* **2017**, *394*, 466−471.
(32) Masuda, H.; Fukuda, K. Ordered Metal Nanohole Arrays Made by a Two-Step Replication of Honeycomb Structures of Anodic Alumina. *Science* **1995**, *268*, 1466−1468.
(33) Lee, S. H.; Lee, J. H.; Park, C.; Kwak, M. K. Roll-Type Photolithography for Continuous Fabrication of Narrow Bus Wires. *J. Micromech. Microeng.* **2016**, *26*, No. 115008.
(34) Chou, S. Y.; Keimel, C.; Gu, J. Ultrafast and Direct Imprint of Nanostructures in Silicon. *Nature* **2002**, *417*, 835−837.
(35) Zhong, H.; Pan, F.; Yue, S.; Qin, C.; Hadjiev, V.; Tian, F.; Liu, X.; Lin, F.; Wang, Z.; Bao, J. Idealizing Tauc Plot for Accurate Bandgap Determination of Semiconductor with Ultraviolet−Visible Spectroscopy: A Case Study for Cubic Boron Arsenide. *J. Phys. Chem. Lett.* **2023**, *14*, 6702−6708.
(36) Farsi, H.; Gobal, F.; Barzgari, Z. A Study of Hydrated Nanostructured Tungsten Trioxide as an Electroactive Material for Pseudocapacitors. *Ionics* **2013**, *19*, 287−294.
(37) Lin, H.-I.; Jeem, M.; Zhang, L.; Watanabe, S. Submerged Photosynthesis of Molybdenum−Tungsten Nanostructures for Supercapacitor Application. *ACS Appl. Nano Mater.* **2023**, *6*, 8325−8334.
(38) Fathi, S.; Sheikhi, M. H.; Zerafat, M. M. Improvement of Plasmonic CuS Nanocrystals' Optoelectronic Properties via Cation Exchange for Infrared Detection Enhancement. *ACS Appl. Electron. Mater.* **2022**, *4*, 2203−2216.
(39) Philippe, L.; Heiss, C.; Michler, J. Electroplating of Stainless Steel. *Chem. Mater.* **2008**, *20*, 3377−3384.
(40) Li, L.; Breedveld, V.; Hess, D. W. Creation of Superhydrophobic Stainless Steel Surfaces by Acid Treatments and Hydrophobic Film Deposition. *ACS Appl. Mater. Interfaces* **2012**, *4*, 4549−4556.
(41) Segets, D.; Gradl, J.; Taylor, R. K.; Vassilev, V.; Peukert, W. Analysis of Optical Absorbance Spectra for the Determination of ZnO Nanoparticle Size Distribution, Solubility, and Surface Energy. *ACS Nano* **2009**, *3*, 1703−1710.
(42) Cui, X.; Ruan, Q.; Zhuo, X.; Xia, X.; Hu, J.; Fu, R.; Li, Y.; Wang, J.; Xu, H. Photothermal Nanomaterials: A Powerful Light-to-Heat Converter. *Chem. Rev.* **2023**, *123*, 6891−6952.
(43) Fillet, R.; Nicolas, V.; Fierro, V.; Celzard, A. Modeling Heat and Mass Transfer in Solar Evaporation Systems. *Int. J. Heat Mass Transfer* **2021**, *181*, No. 121852.
(44) Xue, C.; Huang, R.; Xue, R.; Chang, Q.; Li, N.; Zhang, J.; Hu, S.; Yang, J. Design of Ultrathin TiO_2 Nanosheets Coated Ti Plate for Enhanced Interfacial Solar Driven Water Evaporation Performance. *J. Alloys Compd.* **2022**, *909*, No. 164843.
(45) Cheedarala, R. K.; Song, J. I. Face-Centered Cubic CuO Nanocrystals for Enhanced Pool-Boiling Critical Heat Flux and Higher Thermal Conductivities. *Int. J. Heat Mass Transfer* **2020**, *162*, No. 120391.
(46) Liu, C.; Su, J.; Chang, Q.; Li, Y.; Yang, J.; Hu, S. Electricity-Boosted Solar-to-Vapor Conversion upon Fiber-Supported CDs@CuS for Rapidly Vaporizing Seawater. *Sol. RRL* **2022**, *6*, No. 2200170.
(47) Nishino, F.; Jeem, M.; Zhang, L.; Okamoto, K.; Okabe, S.; Watanabe, S. Formation of CuO Nano-Flowered Surfaces via Submerged Photosynthesis of Crystallites and Their Antimicrobial Activity. *Sci. Rep.* **2017**, *7*, No. 1063.
(48) Matsuo, R.; Takahashi, Y.; Watanabe, S.; Okabe, S. Fabrication of ZnO/CuO Nanoforests and Their Applicability to Microbial Photoelectrochemical Cells. *Appl. Catal., B* **2023**, *339*, No. 123097.

https://doi.org/10.1021/acsomega.4c07571
ACS Omega 2024, 9, 44714−44723